ICARUS **119,** 153–172 (1996)
ARTICLE NO. 0008

The Asymmetric Time-Variable Rings of Mars

DOUGLAS P. HAMILTON*

Max Planck Institut für Kernphysik, Postfach 103980, 69029 Heidelberg, Germany
E-mail: hamilton@astro.umd.edu

Received April 18, 1995; revised August 9, 1995

In this paper, we investigate the dynamics and steady-state behavior of the hypothetical circumplanetary dust rings associated with the two tiny satellites of Mars, Phobos and Deimos. These moonlets are subject to a flux of micrometeoroids which erodes their surfaces and ejects material into orbit around Mars. We study the detailed orbital dynamics of ejected material between a micrometer and a millimeter in radius and find that these grains are significantly perturbed by solar radiation pressure and Mars' oblateness. The coupling between these two forces forms rings that are vertically and azimuthally asymmetric as well as time-variable. Our analytic and numerical results show that material of all sizes launched from Deimos forms a ring that is displaced *away* from the Sun. Grains with radii smaller than ≈270 μm launched from Phobos, however, form a ring that is displaced *toward* the Sun. This effect, as well as surprisingly large orbital changes for Phobos grains, is due to a near resonance between Mars' orbital motion and the precession of pericenter due to the oblateness force. When viewed from along Mars' vernal equinox (the intersection between Mars' orbital and equatorial planes), the ring formed by Deimos grains smaller than ≈100 μm is tilted out of the equatorial plane. We present a new analytical solution describing this vertical asymmetry and interpret it in terms of the Laplace plane. Finally, we suggest that the martian rings may be sustained through the ejecta produced by energetic collisions between ring particles in the 20–50 μm range and the small moonlets Phobos and Deimos.

1. INTRODUCTION

The small particles that make up faint ring systems of the giant planets undergo complex orbital motions due to the large array of forces that act upon them. Besides the strongest gravitational perturbations—those due to the Sun, to the nonsphericity of the primary, and to nearby satellites—micrometer-sized ring particles are also subject to powerful nongravitational perturbations. Principal among these are solar radiation pressure and electromagnetic forces (Hamilton 1993) which have been shown to significantly influence particles in the jovian ring (Burns *et al.* 1985) and in the saturnian E ring (Horanyi *et al.* 1992). Because the strengths of the various perturbation forces vary from one locale to another, dust particles in different locations behave differently and, as a consequence, faint ring systems display a rich variety of structure.

Faint rings are integrally related to small moonlets since the latter act as both sources and sinks for orbiting particles. Rapidly moving meteoroids, originating from interplanetary or interstellar space as well as from the ring itself, strike the moonlets and eject clouds of material. It has long been recognized that such a tenuous ring of circumplanetary debris should exist near the orbits of the two martian satellites Phobos and Deimos (Soter 1971) but, despite several attempts, the putative ring has yet to be unambiguously detected. Using images from the Viking cameras, Duxbury and Ocampo (1988) were able to place an upper limit of $\tau < 3 \times 10^{-5}$ on the ring's normal optical depth. Two years later, Dubinin *et al.* (1990), analyzing early data from the ill-fated Phobos-2 mission, noted that strong solar wind disturbances in the plasma and magnetic fields observations were correlated with the orbit of Phobos. They suggest that these observations are compatible with a ring of gas or dust confined near Phobos' orbit.

The lack of strong observational support has not deterred researchers from attacking the problem analytically. Following Soter (1971), several groups investigated the collisional yield of particles striking Phobos and Deimos. Dobrovolskis and Burns (1980) found that the irregular shape of Phobos, as well as its proximity to Mars, caused the escape velocity from that body to be a strong function of position. Davis *et al.* (1981) extended their analyses to three dimensions finding, for a triaxial Phobos, that the escape velocity over the surface varies between 3.5 and 15.5 m/sec. In a more thorough statistical analysis, Banaszkiewicz and Ip (1991) settled on average values of 7.0 and 5.5 m/sec for Phobos and Deimos, respectively. After escape from the source moonlet, ejecta particles go into circumplanetary orbit around Mars. The subsequent orbital evolution of these grains determines not only the vertical and azimuthal structure of the ring, but also reac-

* Current address: Astronomy Department, University of Maryland, College Park, MD 20742-2421.

0019-1035/96 $12.00

cretion timescales which enter into optical depth calculations. Thus a detailed understanding of orbital dynamics is a necessary prerequisite to predicting the gross features of the martian rings.

Interestingly, the interaction of primarily two perturbation forces—radiation pressure and Mars' oblateness—dominates the evolution of micrometer- to millimeter-sized grains launched from Phobos and Deimos. For smaller grains, electromagnetic perturbations from the weak interplanetary field also need to be considered (Horanyi *et al.* 1990, 1991). Gravitational perturbations from the Sun, from the planets, and from Phobos and Deimos can be ignored in all but a few special cases.

Most of the previous studies of the dynamics of dust around Mars have neglected the oblateness force (e.g., Horanyi *et al.* 1990, 1991, Juhasz *et al.* 1993, Krivov 1994, Ishimoto and Mukai 1994), an omission which radically affects the resulting dynamics. Kholshevnikov *et al.* (1993) studied the dynamics of grains including perturbations from oblateness but not radiation pressure which limits their results to large grains. This study, and several others undertaken independently (Juhasz and Horanyi 1995, Krivov *et al.* 1995, Ishimoto 1995), treat the full problem including both radiation and oblateness forces.

In this work, we focus on the structure of the putative martian rings as a function of particle size. Our approach to the full problem is in stages. We first elucidate the dynamics with a simple analytic model valid for low orbital eccentricities and inclinations and a circularly orbiting Mars. Then we numerically integrate the equations of motion for grains between a micrometer and a millimeter in radius under a variety of different assumptions. We find that, with the addition of four numerically determined parameters, our analytic model can be generalized to a semianalytic model that accounts for the complexities introduced by large orbital eccentricities and inclinations. The nonzero inclinations of Phobos and Deimos, shadowing by Mars, small initial eccentricities, and the effect of launch at different seasons are all relatively unimportant. Unfortunately, the substantial martian eccentricity $e_{\rm Mars} = 0.0934$ cannot be so easily accommodated. Our approach is to investigate the $e_{\rm Mars} = 0$ case in full detail, using both analytic and numerical methods. We then use insight gained from further numerical integrations to discuss changes when $e_{\rm Mars} \neq 0$. We find that our semianalytic model provides reasonable guidance to the full problem.

2. AZIMUTHAL STRUCTURE

2.1. Equations of Motion

To numerically follow the orbital motion of a single dust particle, it is sufficient to integrate Newton's $\mathbf{F} = m\mathbf{a}$ in cartesian coordinates over the time period of interest. More intuition can be gained, however, by looking at the orbital elements which describe a particle's path geometrically. Due to the fact that the perturbation forces are much weaker than Mars' point-source gravity, these parameters have the advantage of changing relatively slowly in time, which allows us to average the perturbation forces over a single orbit. Use of the resulting orbit-averaged equations of motion allows the character of the perturbation and the types of possible orbital evolution to be more easily assessed.

Many choices of orbital elements are possible; the ones that we use here are based on the following set. The semimajor axis a gives the size of an orbit, the eccentricity e is related to its shape, the inclination i indicates the tilt of the orbital plane relative to Mars' equatorial plane, the longitude of the ascending node Ω describes the orientation of the orbital plane, and the argument of pericenter ω determines the orientation of the elliptical orbit within this plane. Further description of the orbital elements can be found in Hamilton (1993, Fig. 1) and in basic celestial mechanics texts (e.g., Danby 1988). For problems in which radiation pressure is important, it is useful to define the solar angle,

$$\phi_\odot = \Omega + \omega - n_\odot t - \delta \tag{1}$$

(Hamilton 1993, Eq. 28), where $n_\odot = 3.341$ rad/yr is the mean motion of Mars, t is time, and δ is a constant. For moderately inclined orbits, $\phi_\odot$ is roughly the angle between orbital pericenter and the Sun as seen from Mars.

An additional advantage of the orbital elements is that if the inclination i and planetary obliquity γ are not too large, the changes in the orbital elements that determine azimuthal structure (e, $\phi_\odot$) are independent of those that determine vertical structure (i, Ω). This approximation holds when both i and γ are less than about 30° (for Mars $\gamma = 25.2°$). Thus the azimuthal and vertical elements can be treated separately; in this section we investigate the azimuthal group adopting the orbit-averaged equations of Hamilton (1993),

$$\left\langle \frac{da}{dt} \right\rangle = 0 \tag{2}$$

$$\left\langle \frac{de}{dt} \right\rangle = \alpha(1-e^2)^{1/2} \sin\phi_\odot \tag{3}$$

$$\left\langle \frac{d\phi_\odot}{dt} \right\rangle = \frac{\alpha(1-e^2)^{1/2}\cos\phi_\odot}{e} + \dot{\tilde{\omega}}_{\rm T}. \tag{4}$$

Here α is a frequency that depends on particle properties and determines the strength of radiation pressure. The constant is inversely proportional to the particle's radius s and increases as the square root of its semimajor axis (i.e., $\alpha \sim a^{1/2}/s$). For a more general definition, see Hamil-

TABLE I
Properties of Phobos and Deimos

Object	a_{moon} (R_{Mars})	e_{moon}	i_{moon} (°)	R_{moon} (km)	v_{esc} (m/s)	v_{circ} (km/s)	τ (days)	τ_{J2} (years)	τ_{col} (years)
Phobos	2.76	0.00	1.0	12	7	2.1	0.32	2.3	29
Deimos	6.91	0.00	1.0	7	5.5	1.4	1.26	56	2100

Note. a_{moon}, e_{moon}, and i_{moon} are the orbital semimajor axis, eccentricity, and inclination adopted for this study; R_{moon} is the average radius; v_{esc} is the adopted normalized escape velocity; v_{circ} is the moon's orbital velocity; τ is the obital period; τ_{J2} is the precision period due to oblateness; and τ_{col} is a recollision timescale for $i = 1°$ orbits.

ton (1993, Eq. 4 and text after Eq. 10f). The rate at which the solar angle $\phi_\odot$ would change in the absence of radiation pressure is given by

$$\dot{\tilde{\omega}}_T = \frac{3nJ_2R_{Mars}^2}{2a^2(1-e^2)^2} - n_\odot, \tag{5}$$

where n is the dust grain's orbital mean motion, $R_{Mars} = 3393$ km is the equatorial radius of Mars, and $J_2 = 0.001960$ is a dimensionless measure of its oblateness. The first term in Eq. (5) is the pericenter precession rate due to planetary oblateness (Danby 1988) and the second is due to the motion of Mars about the Sun.

In addition to being valid for low inclinations only, these expressions assume that Mars' orbit is circular and ignore the martian shadow (i.e., radiation pressure does not shut off in the shadow). Our numerical integrations indicate that shadowing effects cause only minor changes, so they can be neglected with impunity. These numerical integrations also show, however, that Mars' substantial eccentricity is important. It affects Eqs. (1)–(5) by causing $n_\odot$ and α to be periodic functions of time rather than constants. These complications make Eqs. (1)–(5) analytically intractable, so we take $e_{Mars} = 0$ for the moment and return later to discuss the consequences of this assumption.

Equation (2) can be solved immediately: a remains constant (nearly constant if we also consider shadowing—see Mignard 1984). If we make the assumption of small orbital eccentricities e, then $\dot{\tilde{\omega}}_T$ is also constant and Eqs. (3) and (4) can be solved analytically (Horanyi and Burns 1991). It is also possible to find an exact solution when the $(1 - e^2)^{1/2}$ terms are kept in Eqs. (3) and (4), but dropped from Eq. (5) (Hamilton and Burns 1992, Juhasz and Horanyi 1995). In the interest of simplicity, and because the neglected term is often more important than the kept ones, we adopt the low-eccentricity solution here. Debris launched from the martian satellites Phobos and Deimos begin on nearly circular orbits: $e(t = 0) \approx v_{esc}/v_{circ} \approx 0.003$—see Table I. It is, therefore, an excellent approximation to adopt, for $e = 0$ at $t = 0$, the solution

$$e = \frac{2\alpha}{\dot{\tilde{\omega}}_T} \sin \frac{\dot{\tilde{\omega}}_T t'}{2} \tag{6}$$

$$\phi_\odot = \frac{\dot{\tilde{\omega}}_T t'}{2} + \frac{\pi}{2}, \tag{7}$$

where $t' = t$ modulo $2\pi/|\dot{\tilde{\omega}}_T|$ and t is time. The eccentricity oscillates sinusoidally as the angle between pericenter and the Sun changes uniformly from 90° to 270°. Depending on the sign of $\dot{\tilde{\omega}}_T$, $\phi_\odot$ either precesses through 180° or regresses through 0°. The angle reaches 270° just as the eccentricity returns to zero, at which point the angle "jumps" back to 90° to begin the cycle anew. This jump is a result of the first term on the right-hand side of Eq. (4); for nearly circular orbits, this term dominates and radiation pressure rapidly drives $\phi_\odot$ to 90°.

The solution can also be understood geometrically in terms of free and forced eccentricities (see Horanyi and Burns 1991, Fig. 2). The forced eccentricity is the eccentricity at the stationary point of Eqs. (3) and (4), which depends solely on the strengths of the perturbation forces. It can be found numerically for arbitrary eccentricity and reduces to

$$e_{forced} = \frac{\alpha}{|\dot{\tilde{\omega}}_T|} \tag{8}$$

for $e \ll 1$. The free eccentricity is the amplitude of the oscillation about this value which is determined by initial conditions. With our choice of initial conditions ($e = 0$ at $t = 0$), $e_{free} = e_{forced} = e_{max}/2$. This view allows the more general case $e_{free} \neq e_{forced}$ to be easily visualized.

2.2. Numerical Simulations

The simple analytic solution presented above holds up reasonably well against numerical simulations for most grains launched from Deimos (still assuming $e_{Mars} = 0$). Figure 1 shows the orbital evolution of a 40 μm dust grain started on an initially circular orbit from the outer martian moonlet. The semimajor axis typically displays short-pe-

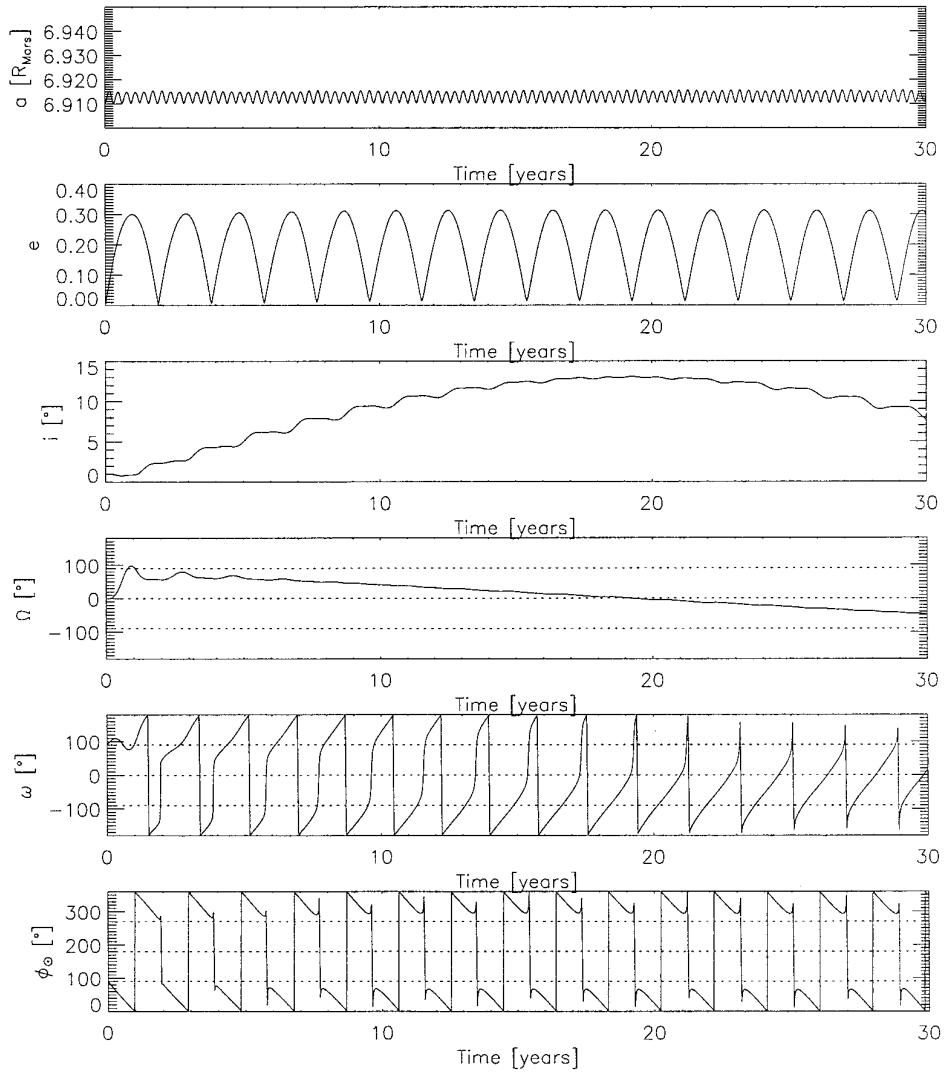

FIG. 1. The orbital history of a dust grain 40 μm in radius launched from the martian moon Deimos. We integrate Newton's equation in planet-centered Cartesian coordinates and include the point-source and J_2 terms of the martian gravity field as well as solar radiation pressure (without shadowing); Mars' eccentricity is artificially set to zero. For the dust, we assumed spherical particles with density $\rho = 2.38$ g/cm^3 and light scattering efficiency $Q_{\rm pr} = 1$. The first five panels show the time behavior of the osculating elements which describe the orbital size (semimajor axis), shape (eccentricity), and spatial orientation (inclination, longitude of the ascending node, argument of pericenter) as a function of time. The sixth panel is the solar angle $\phi_\odot$ described in the text.

riod oscillations (real, but the period is artificially long due to our sampling rate) and a gradual increase with time (numerical error). The linear increase is not visible in Fig. 1, which indicates that numerical errors in the other elements are small as well. We routinely monitor the semimajor axis as a check on the accuracy of our integrations. The periodic oscillation has a small amplitude and hence, to a good approximation, the semimajor axis remains constant in time, in agreement with Eq. (2). The eccentricity oscillates sinusoidally in time as the solar angle regresses nearly linearly from 90° to 270° as predicted by Eqs. (6) and (7). The eccentricity returns to zero just as the solar angle reaches 270°, the angle spins rapidly to 90°, and the cycle repeats.

Slight deviations from this simple picture arise from the large inclinations attained by small Deimos grains. As the inclination climbs, the solar angle displays slightly nonlinear behavior (the wiggles in the sixth panel of Fig. 1 become a bit more curved). Nonlinear behavior is more evident in Fig. 2, however, which shows the orbital evolution of a 40 μm grain launched from Phobos. The semimajor axis remains roughly constant, but the eccentricity variations are clearly not sinusoidal. The departures from sinusoidal curves arise in part from $(1 - e^2)^{1/2}$ terms in Eq. (3) which

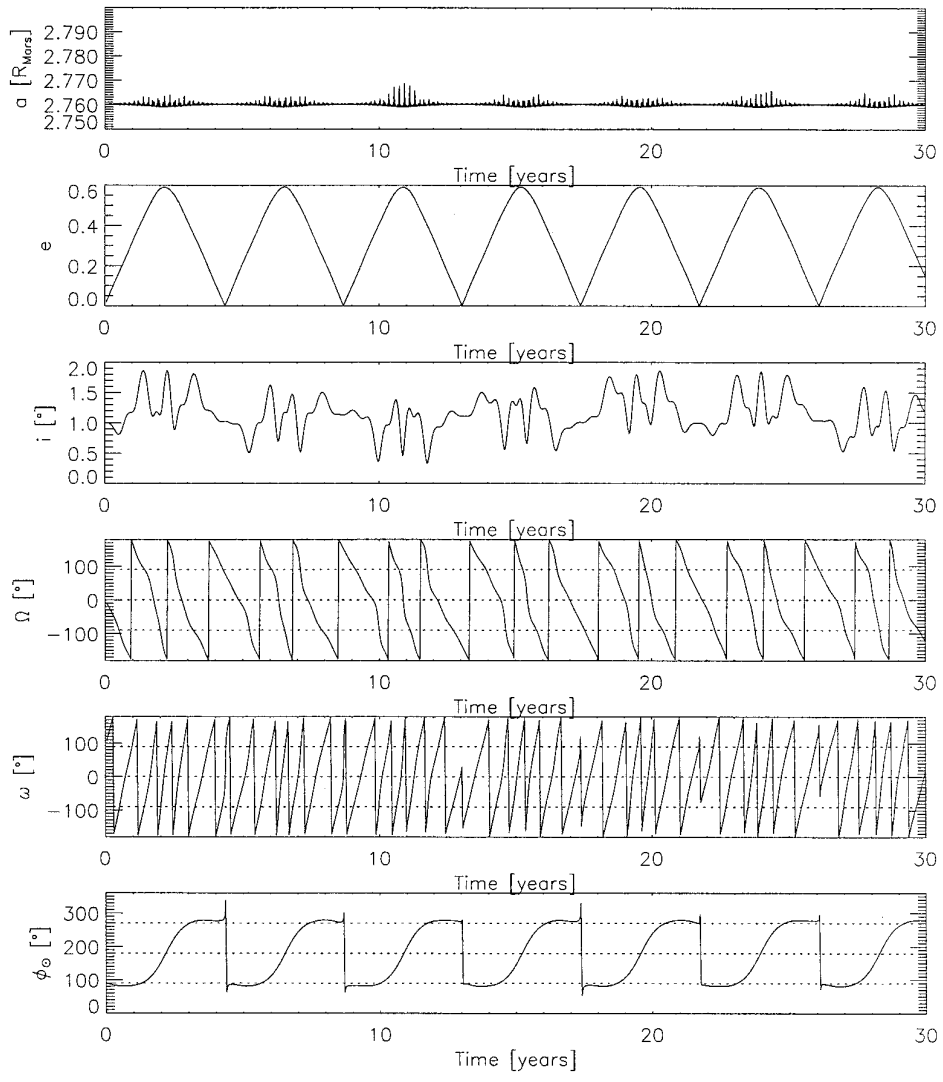

FIG. 2. The orbital history of a 40 μm grain launched from Phobos. We make the same assumptions as in Fig. 1, and plot the same quantities. Compare the eccentricity and solar angle profiles with those of Fig. 1.

were ignored in the low-eccentricity solution, but mainly from the strongly nonlinear evolution of the solar angle (Fig. 2, Eqs. (4) and (5)). In Fig. 2, this angle precesses from 90° to 270° in 4.5 years, taking more than twice as long as its Deimos counterpart to complete one cycle. Thus somewhat paradoxically, the Phobos grain attains a higher eccentricity despite the fact that radiation pressure is a stronger perturbation at Deimos. The differences in the evolution of the solar angle for Phobos and Deimos grains have other interesting consequences for the azimuthal structure of the martian ring which we now investigate.

To make the differences more clear, we substitute martian parameters into Eq. (5) and obtain the following expressions:

$$\text{Phobos: } \dot{\tilde{\omega}}_T \text{ (rad/yr)} = \frac{2.780}{(1-e^2)^2} - 3.341 \tag{9}$$

$$\text{Deimos: } \dot{\tilde{\omega}}_T \text{ (rad/yr)} = \frac{0.1120}{(1-e^2)^2} - 3.341. \tag{10}$$

For Deimos, the term due to Mars' oblateness is negligible for all but the highest eccentricities (see Table II). Thus in Fig. 1 the solar angle regresses nearly linearly and the period of the eccentricity oscillation is just ≈4% longer than Mars' orbital period of 1.88 yr. The situation for Phobos, however, is quite different. Phobos' precession period is nearly equal to Mars' orbital period and dust launched from Phobos is strongly affected by this near

TABLE II
Critical Eccentricities and Grain Radii

Object	e_{impact}	s_{impact}	e_{cross}	s_{cross}	e_{crit}	s_{crit}
Phobos	0.638	26 μm	—	—	0.298	270 μm
Deimos	0.855	13 μm	0.601	20 μm	0.904	—

Note. Here e_{impact}, e_{cross}, and e_{crit} are the eccentricities at which particles are lost to Mars, cross the orbit of the other satellite, and cause the precession rate to equal zero, respectively (s_{impact}, s_{cross}, and s_{crit} are the corresponding grain radii).

commensurability. Eccentricities grow larger than they would in the absence of oblateness because this term drastically reduces the size of $|\dot{\tilde{\omega}}_{\text{T}}|$ (see Eq. (6)). Furthermore, strong nonlinear effects occur for moderate eccentricities. In Fig. 2, for example, the solar angle regresses for the first year or so as the eccentricity grows. When the eccentricity exceeds a critical value, e_{crit}, the nonlinear terms cause Eq. (9) to change sign and the solar angle begins to precess. For Phobos, $e_{\text{crit}} \approx 0.3$ (see Table II).

Whether the solar angle regresses through 0° (as in Fig. 1) or precesses through 180° (as in Fig. 2) has an important effect on the structure of the ring. As can be seen from Eq. (3) and Figs. 1 and 2, the eccentricity always increases when $0° < \phi_{\odot} < 180°$ and always decreases when $180° < \phi_{\odot} < 360°$. If the solar angle regresses through 0°, as in Fig. 1, the maximum eccentricity always occurs at $\phi_{\odot} = 0°$. If, on the other hand, the solar angle precesses through 180° as in Fig. 2, then $\phi_{\odot} = 180°$ when the eccentricity is maximum. Since $\phi_{\odot}$ measures the angle between the Sun and the orbit's pericenter, the most distant material will be found offset away from the Sun in the first case (Deimos) and toward the Sun in the second (Phobos).

This effect shows up clearly in Fig. 3. More than 20,000 orbital positions were obtained from the orbits displayed in Figs. 1 and 2, then projected into the martian equatorial plane, and finally plotted in a coordinate system where the Sun is always located along the positive x_{rot}-axis. The positions shown in this diagram are traced out by a single particle launched from each moon and followed over a period of time; this is, in general, different from a snapshot taken of a real ring (i.e., an ensemble of particles launched at different times). If, however, the forces operating on a

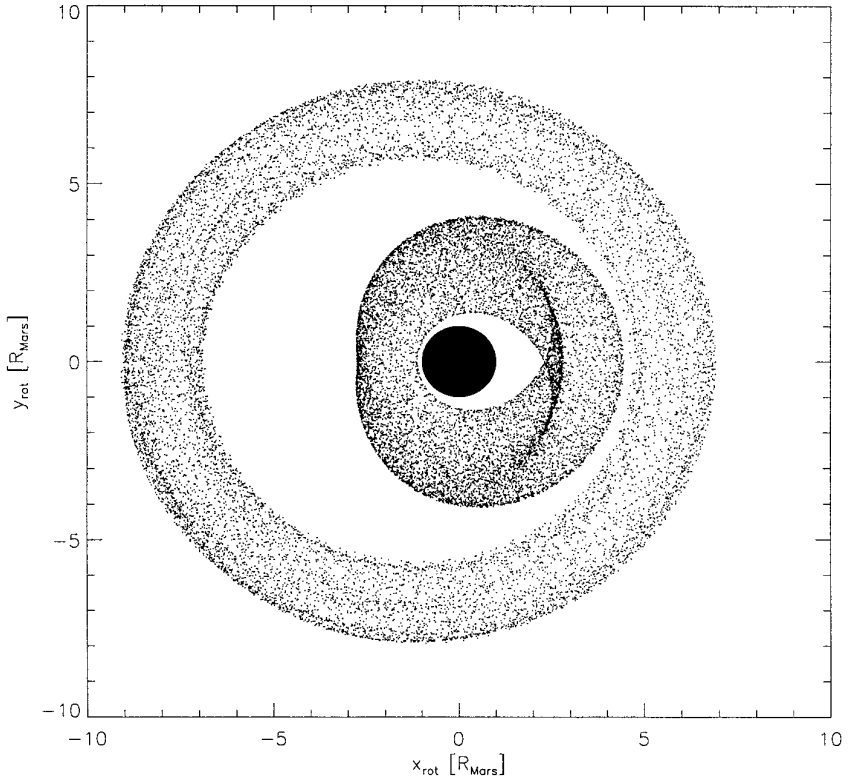

FIG. 3. The rings formed by 40 μm grains launched from Phobos and Deimos. Particles have been projected into the martian equatorial plane and are plotted in a coordinate system that rotates with Mars' mean motion around the Sun. Thus in this diagram, the Sun is always located out along the positive x_{rot}-axis and the ring is mirror-symmetric about the x_{rot}-axis. Grains launched from Deimos attain their maximum eccentricities when the solar angle is near zero (Fig. 1); hence the Deimos ring is displaced away from the Sun. For Phobos, maximum eccentricities are reached when the solar angel is near 180° (Fig. 2), so the Phobos ring is offset toward the Sun.

grain are independent of the particle's launch time, then the two constructs are identical. This is nearly the case for the martian dust rings if $e_{\rm Mars} = 0$.

We can approximate the shape of the Deimos ring analytically by taking the low-eccentricity solution (Eqs. (6) and (7)) and solving for the outer and inner envelopes that enclose the ring. To second order in the eccentricity, this exercise yields circular envelopes of radii $a(1 \pm e_{\rm forced})$ offset by $ae_{\rm forced}$ away from the Sun (recall that $e_{\rm max} = 2e_{\rm forced}$ for our initial conditions). Thus Deimos skims the outer edge of its ring when the moon is closest to the Sun and the inner edge when it is farthest from the Sun. From the analytic solution, we predict that Deimos grains 40 microns in size form a ring $2ae_{\rm forced} \approx 2.1R_{\rm Mars}$ wide offset away from the Sun by $ae_{\rm forced} \approx 1.0R_{\rm Mars}$, numbers that are in good agreement with Fig. 3. This simple calculation is less successful for Phobos because of the nonlinear $(1 - e^2)^{1/2}$ terms in the precession rate. Note however, the interesting density enhancement in Fig. 3 to the right of Mars at about Phobos' distance ($2.76R_{\rm Mars}$). The feature is real and arises from the fact that over much of the orbit, the solar angle has values near 90° and 270° (Fig. 2).

Up to this point we have only considered rings composed of a single grain size, but in reality ejecta lifted off the martian moons will contain a range of particle sizes. We have also seen that particles may form rings that are offset either away from or toward the Sun based on whether the solar angle regresses through 0° or precesses through 180°. To estimate how rings composed of different sized particles will look, we need to know both the maximum eccentricity (which determines the ring's width and the magnitude of its offset) and the solar angle at maximum eccentricity (which determines the direction of the offset) for each particle size. In addition, the period of the eccentricity oscillation is a sensitive indicator of the importance of the nonlinear oblateness term. For longer eccentricity periods, oblateness plays a more important role and the ring is more likely to have a complicated structure.

These three quantities are plotted in Fig. 4 for spherical ejecta particles with $Q_{\rm pr} = 1$, $\rho = 2.38$ g/cm^3, and radii between a micrometer and a millimeter. The information contained in Fig. 4 has been distilled from nearly 500 different initial conditions which were numerically integrated for 50 years (several tens of thousands of orbits about Mars—see Table I). Note that the two solid curves, which represent particles launched at Mars' summer and winter solstices, lie atop one another as do the two dashed lines representing particles launched at the spring and autumn equinoxes. In addition, the solid and dashed curves also lie near each other. Taken together, these results indicate that the effects of the martian seasons are relatively unimportant and that the small inclinations of the martian moonlets are entirely negligible in determining the azimuthal structure of the rings. Thus particles launched at different times undergo similar dynamics and, as discussed above, the time history of a single particle (i.e., Fig. 3) provides a good approximation to the structure of the real ring.

The left-hand side of Fig. 4's top panel shows that grains smaller than a cutoff size, $s_{\rm impact}$, attain the large eccentricities, $e_{\rm impact}$, necessary to strike Mars. Our cutoff size for Phobos grains, $s_{\rm impact} = 26$ μm (Table II), is significantly larger than that determined by Juhasz *et al.* (1993) because their calculations do not include the effects of the martian oblateness. What else does Fig. 4 tell us about grains with $s < s_{\rm impact}$? The time between launch and collision with Mars can be read from the second panel—particles smaller than about 10 μm, for example, remain in the martian ring for less than 1 yr. For particles that strike Mars, the third panel shows the angle between the Sun and the impact point. Thus Deimos grains strike the planet roughly between the dusk terminator (the tiniest particles) and local noon (larger impacters) while Phobos grains hit between the dusk terminator (the smallest particles) and local midnight (larger impacters). These grains are not large enough to produce visible martian meteors (Adolfsson *et al.* 1996); indeed, the smallest are rapidly slowed by the martian atmosphere and probably float down to the martian surface relatively unscathed.

The right-hand side of Fig. 4 gives orbital data for particles that avoid colliding with Mars. As a result of the martian oblateness, all particles launched from Phobos attain larger eccentricities than their counterparts launched from Deimos. The period of the eccentricity oscillation varies dramatically for Phobos grains of different sizes, but remains constant at about 1.95 yrs for Deimos grains; the former are strongly affected by oblateness while the latter are only slightly influenced. In addition, note that the ratio of the Phobos period to the Deimos period approaches six for large grains in agreement with the low-eccentricity limit of Eqs. (9) and (10). The final panel shows that the Phobos ring is offset toward the Sun for grain sizes between 26 and 270 μm; for larger grains, the Phobos ring is offset away from the Sun as is the Deimos ring for all grain sizes.

The most striking feature in all three panels of Fig. 4 occurs for Phobos at a particle size of about 270 μm. Here the maximum eccentricity takes a precipitous drop, the eccentricity period peaks, and the solar angle at maximum eccentricity flips 180°. The behavior is integrally related to the history of the solar angle. For grains just to the left of the peak in Fig. 4's second panel (e.g., the 250 μm grains in Fig. 5), the solar angle regresses, levels out just above $\phi_\odot = 0°$, and then precesses when the eccentricity grows larger than $e_{\rm crit}$ (Table II). The eccentricity continues to increase as long as $0° < \phi_\odot < 180°$. To the right of the peak in Fig. 4, the behavior is initially similar, but the solar angle reaches 0° before the eccentricity attains $e_{\rm crit}$. Thus the solar angle slips across 0° and the eccentricity decreases.

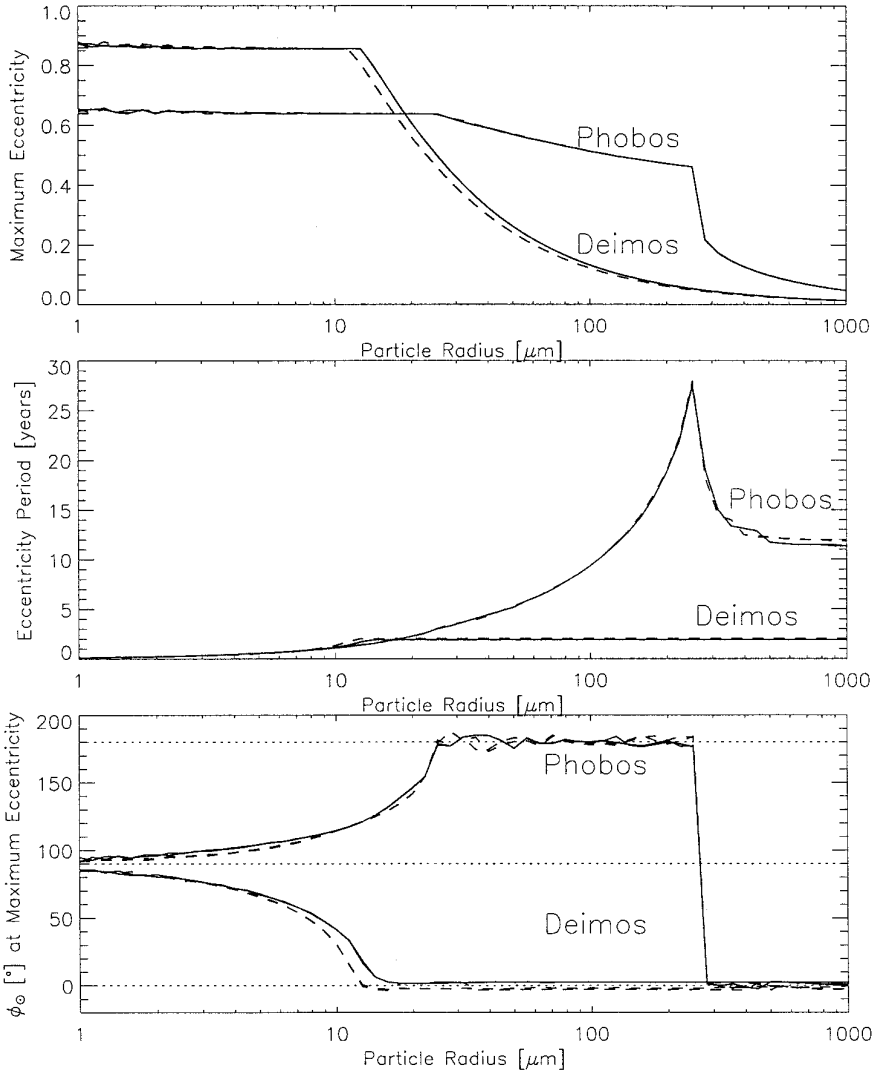

FIG. 4. Orbital properties of Phobos and Deimos ejecta as a function of particle size. Nearly 500 initial conditions are represented here: each of the three panels contains, for each moon, a set of four curves through 61 points. The curves correspond to grains of different sizes launched at different points along the martian orbit: the spring and autumn equinoxes (dashed) and the summer and winter solstices (solid). The quantities displayed here, and hence the azimuthal structure of the ring, are relatively insensitive to the launch time. (a) Maximum eccentricity. The flat part of the curves to the left indicate that particles collide with Mars. (b) Period of the eccentricity oscillation. The effects of the near resonance for Phobos are clearly noticeable. (c) Solar angle. The ring formed by all Deimos ejecta is displaced away from the Sun, as is the ring created by Phobos grains larger than 270 μm. In contrast, Phobos grains smaller than 270 μm are displaced toward the Sun.

For these grains, $e_{\max} < e_{\text{crit}}$ and the eccentricity period is shorter since the solar angle never precesses. Very similar behavior was investigated in Hamilton (1993)'s study of Saturn's E ring (see his Figs. 3 and 4). The situation in the E ring is more complicated since the solar angle is also affected by electromagnetic perturbations.

Figure 4 can also be used to predict the structure of the rings formed by particles of a given size. We take grains of 250 μm as an extreme example. The situation is simple for Deimos: the maximum eccentricity of 0.05 (Fig. 4, panel 1) is well below e_{crit} (Table II), so the ring is circular with a width of $2ae_{\text{forced}} \approx 0.35R_{\text{Mars}}$, offset by $ae_{\text{forced}} \approx 0.17R_{\text{Mars}}$ away from the Sun. For Phobos, $e_{\max} \approx 0.45$ occurs for $\phi_{\odot} = 180°$, so the ring should be offset toward the Sun. Its shape and structure will be strange, however, as indicated by the large eccentricity period which arises from nonlinearities. Rather than predicting a width of $2ae_{\text{forced}} \approx 1.2R_{\text{Mars}}$, we assume that the nonlinear evolution of the solar angle will smear the ring out to about $a(1 + e_{\max}) - a(1 - e_{\max}) = 2ae_{\max} \approx 2.5R_{\text{Mars}}$. We plot the ring created

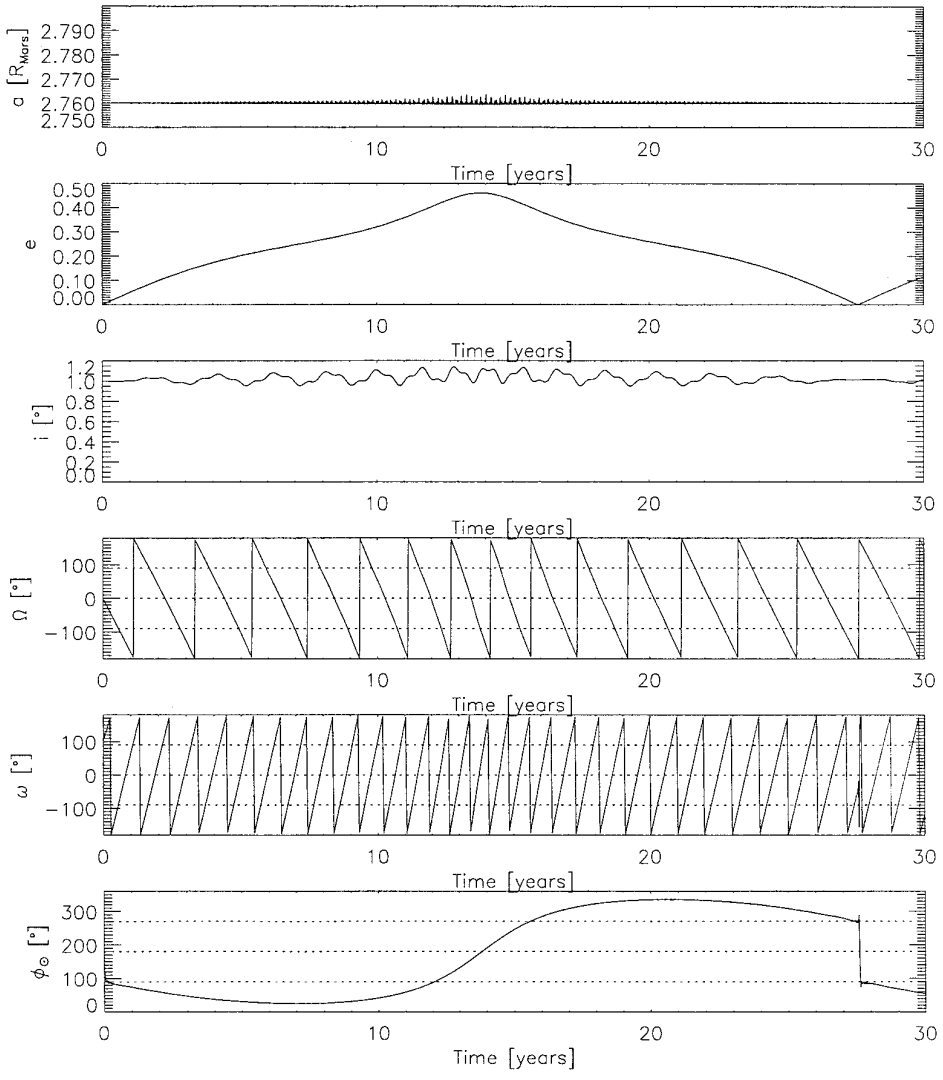

FIG. 5. The orbital history of a 250 μm grain launched from Phobos. We make the same assumptions as in Fig. 1, and plot the same quantities. Compare the eccentricity and solar angle profiles with those of Fig. 2.

by 250 μm particles launched from Phobos and Deimos in Fig. 6 (cf. Fig. 3). The Deimos ring matches its description very well, and the Phobos ring extends more toward the Sun, is about $2.5R_{\rm Mars}$ wide, and has an odd structure as expected. Furthermore, strong density enhancements are clearly visible in the Phobos ring, the detailed structure of which can be understood from Fig. 5. In Fig. 5, the solar angle spends a relatively large amount of time near 30° and 330°, thereby creating the density enhancements in Fig. 6. This dense ''core,'' which is about $1.2R_{\rm Mars}$ wide and offset away from the Sun, is also present for grains larger than $s_{\rm crit} \approx 270$ μm. The faint sunward component in Fig. 6 is due to the rapid precession through $\phi_\odot = 180°$; it does not occur for the larger particles.

3. VERTICAL STRUCTURE

3.1. Equations of Motion

To fully characterize the structure of the martian ring, we must also consider perturbations to the orbital elements that determine vertical structure, namely i and Ω. As in the previous section, we begin with the equations of motion. As motivation, however, please reconsider the three orbital histories displayed in Figs. 1, 2, and 5. Although the Phobos grains display complex inclination traces, the magnitude of the changes are limited to less than a degree and to a few tenths of a degree in Figs. 2 and 5, respectively. Changes of this magnitude do not substantially alter the vertical

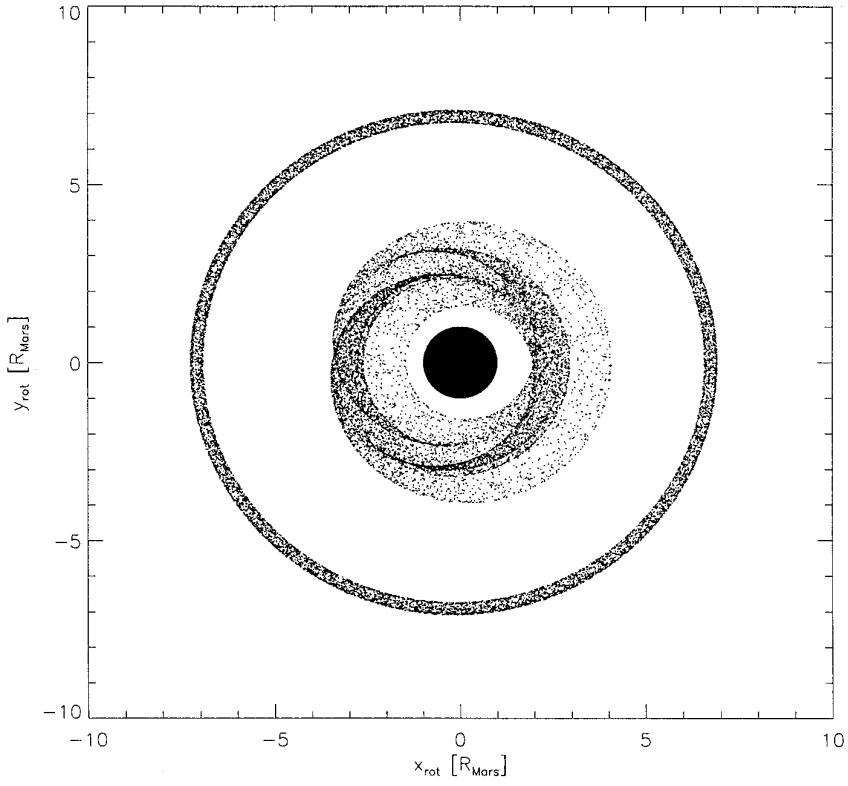

FIG. 6. The rings formed by 250 μm grains launched from Phobos and Deimos as seen in a coordinate system rotating with the Sun's mean motion. In this frame, the Sun is out along the positive x_{rot}-axis. Deimos grains remain on very circular orbits while Phobos grains form a broad and highly-distorted ring.

structure of the Phobos ring. For 40 μm grains from Deimos (Fig. 1), however, the inclination rises to a significant 13° in what appears to be a simple sinusoidal pattern (see also the first two traces of Fig. 7). The magnitude of this change provides proof that vertical structure is important for the Deimos ring while the simplicity of the curve gives hope that an analytic solution might be found.

The orbital equations governing a ring's vertical structure subject to radiation pressure, oblateness, and electromagnetism can be found in Hamilton (1993). We start with the full set of orbit-averaged equations and neglect terms of second-order in the inclination and martian obliquity $\gamma = 25.2°$ (e.g., $\cos i \approx \cos\gamma \approx 1$). The resulting equations are identical to Hamilton (1993)'s Eqs. 27–32, with the exception of an additional term in the equation for Z. This extra term results from relaxing Hamilton (1993)'s assumption of $i \ll \gamma$. We find that

$$\left\langle \frac{di}{dt} \right\rangle = Z \cos\omega \tag{11}$$

and

$$\left\langle \frac{d\Omega}{dt} \right\rangle = Z \frac{\sin\omega}{\sin i} + \dot{\Omega}_{xy}, \tag{12}$$

where Z and $\dot{\Omega}_{xy}$ are given by

$$Z = \frac{\alpha e}{(1-e^2)^{1/2}} [\sin\gamma \sin(n_\odot t + \delta) + \sin i \sin(\Omega - n_\odot t - \delta)] \tag{13}$$

and

$$\dot{\Omega}_{xy} = -\frac{3nJ_2R_{\rm Mars}^2}{2a^2(1-e^2)^2}. \tag{14}$$

Hamilton (1993) derived an approximate solution for these equations valid for very small inclinations ($\lesssim 2°$ for 40 μm Deimos grains), but we are clearly interested in much larger inclinations here (Fig. 1). The apparent simplicity of expressions (11) and (12) is deceiving. Most of the complexity in the equations governing vertical structure is contained in Z and ω, which depend on the previously discussed solution for the azimuthal elements e and $\phi_\odot$. Since the previous solution (Eqs. (6) and (7)) was valid only for small eccentricities, we make the same approximation here by neglecting e^2 terms. We proceed by replacing e with the right-hand side of Eq. (6) in Eq. (13) and substituting the result into Eqs. (11) and (12). We eliminate ω

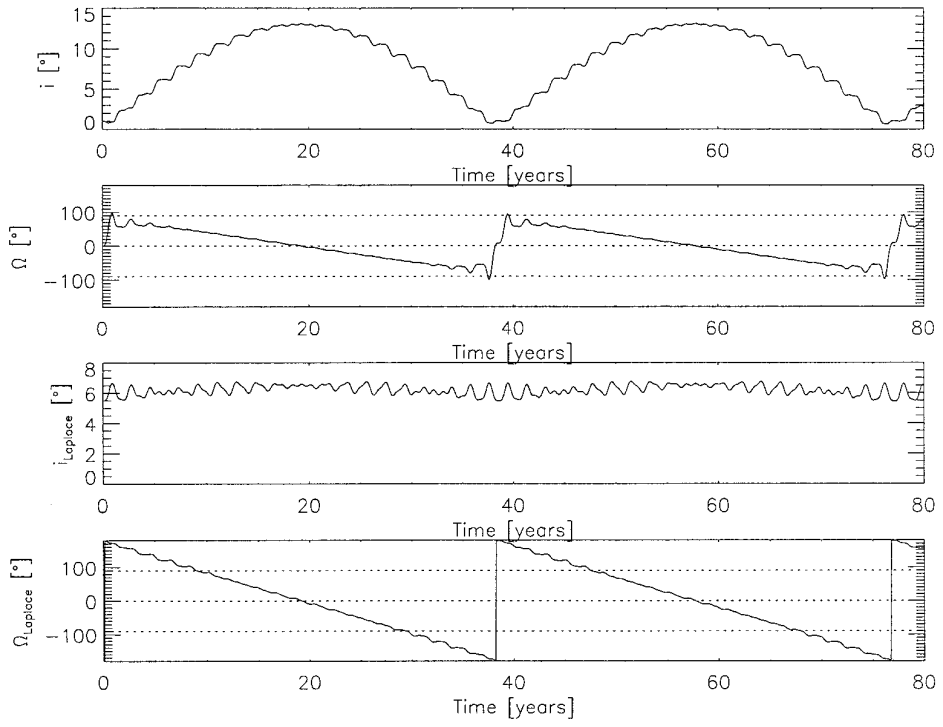

FIG. 7. Inclination and ascending node traces for the orbit in Fig. 1. The first two panels show the elements relative to Mars' equatorial plane, but over a longer period of time than in Fig. 1. The third and fourth panels show the inclination and ascending node measured relative to an approximate Laplace plane tilted by $i_{\text{forced}} \approx 6.5°$ from the equatorial plane toward the ecliptic. As measured from the Laplace plane, the inclination is approximately constant and the node precesses at a nearly constant rate.

from Eqs. (11) and (12) with Eq. (1) and, finally, $\phi_\odot$ from the resulting expressions with Eq. (7). We find that

$$\left\langle \frac{di}{dt} \right\rangle = -\frac{2\alpha^2}{\dot{\tilde{\omega}}_T} \sin\left(\frac{\dot{\tilde{\omega}}_T t}{2}\right) \sin\left(\frac{\dot{\tilde{\omega}}_T t}{2} - \Omega + n_\odot t + \delta\right) \tag{15}$$
$$[\sin\gamma \sin(n_\odot t + \delta) + \sin i \sin(\Omega - n_\odot t - \delta)]$$

and

$$\left\langle \frac{d\Omega}{dt} \right\rangle = \frac{2\alpha^2}{\dot{\tilde{\omega}}_T \sin i} \sin\left(\frac{\dot{\tilde{\omega}}_T t}{2}\right) \cos\left(\frac{\dot{\tilde{\omega}}_T t}{2} - \Omega + n_\odot t + \delta\right) \tag{16}$$
$$[\sin\gamma \sin(n_\odot t + \delta) + \sin i \sin(\Omega - n_\odot t - \delta)] + \dot{\Omega}_{xy}.$$

These expressions are self-contained, depending only on i, Ω, t, and the constant and nearly constant quantities α, γ, $\dot{\tilde{\omega}}_T$, $\dot{\Omega}_{xy}$, $n_\odot$, and δ. Unfortunately each equation contains products of three sinusoidally varying terms which complicates the form of a general solution. The product of three sinusoids, however, can be rewritten as the sum of four sines and cosines with identical amplitudes, and arguments formed from sums and differences of the original arguments. If the regression of the node Ω is slow ($\gtrsim$5 years), then three of the resulting terms circulate on year to two-year timescales, while the fourth varies more slowly with Ω. This inequality is clearly satisfied for grains from Deimos (see Fig. 7), but not for those from Phobos (see Figs. 2 and 5). Since the amplitudes of each of the four summed sinusoidal terms are equal, the Ω terms will dominate simply because they cause monotonic changes for a longer period of time. We therefore make the final approximation and neglect the short-period terms. The expressions simplify to

$$\left\langle \frac{di}{dt} \right\rangle_{\text{long}} = -\frac{\alpha^2 \sin\gamma}{2\dot{\tilde{\omega}}_T} \sin\Omega \tag{17}$$

$$\left\langle \frac{d\Omega}{dt} \right\rangle_{\text{long}} = -\frac{\alpha^2 \sin\gamma}{2\dot{\tilde{\omega}}_T} \frac{\cos\Omega}{\sin i} + \dot{\Omega}_T \tag{18}$$

with

$$\dot{\Omega}_T = \frac{\alpha^2}{2\dot{\tilde{\omega}}_T} + \dot{\Omega}_{xy}. \tag{19}$$

The subscript "long" has been appended as a reminder that these expressions apply to the long-period perturba-

tions only. Now Eqs. (17) and (18) (with $\sin i \approx i$) are identical in form to the low-eccentricity versions of Eqs. (3) and (4). Thus for orbits that are initially uninclined, the solution can be transcribed directly from Eqs. (6) and (7):

$$i_{\text{long}} = -\frac{\alpha^2 \sin\gamma}{\dot{\Omega}_{\text{T}}\dot{\tilde{\omega}}_{\text{T}}} \sin\frac{\dot{\Omega}_{\text{T}} t'}{2} \tag{20}$$

and

$$\Omega_{\text{long}} = \frac{\dot{\Omega}_{\text{T}} t'}{2} + \frac{\pi}{2}. \tag{21}$$

Like the solar angle $\phi_\odot$, the node starts at 90°, after which it moves uniformly to −90° before "jumping" back to 90°. The inclination behaves just as the eccentricity, going through a single sinusoidal oscillation during the precessional cycle. These basic trends show up well in Fig. 7. The one and two year short-period terms neglected in the analytic solution are also evident as "noise" in both the inclination and ascending node traces of Fig. 7.

It is interesting to note that the magnitude of the inclination solution (Eq. (20)) is second order in α, the strength of radiation pressure. This fact was first pointed out by Allan and Cook (1967) in their study of a similar problem. The implication is that inclinations will drop off rapidly for larger particles; amplitudes of a degree should not be exceeded by dust grains larger than about 140 μm in radius. The solution discussed here, therefore, will have relevance for only the small-particle component of the Deimos ring.

Just as for the azimuthal solution, the vertical solution can be interpreted in terms of free and forced parameters—in this case inclinations. The forced inclination is given by

$$i_{\text{forced}} = \frac{\alpha^2 \sin\gamma}{2|\dot{\Omega}_{\text{T}}\dot{\tilde{\omega}}_{\text{T}}|}. \tag{22}$$

For orbits that begin with $i = 0$, $i_{\text{free}} = i_{\text{forced}} = i_{\max}/2$. Solutions for different initial condition correspond to different values of i_{free}. The actual inclination, then, varies periodically between $i_{\min} = |i_{\text{forced}} - i_{\text{free}}|$ and $i_{\max} = i_{\text{forced}} + i_{\text{free}}$. In the azimuthal solution for e and $\phi_\odot$, the martian rings are offset by ae_{forced} toward or away from the Sun. Since we are interested in the vertical structure of the Deimos ring, it is worthwhile to interpret i_{forced} geometrically.

The oblateness perturbation, acting on an orbit in Mars' equatorial plane, is a purely equatorial force which does not affect an orbit's inclination. Similarly, solar gravity and solar radiation pressure exert no out-of-ecliptic forces on circumplanetary orbits confined to the ecliptic plane. When planetary and solar forces are combined, however, dust grain orbits do not remain in either the equatorial or the ecliptic plane. Nevertheless, for a dust grain with given physical properties on a Keplerian orbit, there exists a unique plane—the Laplace plane—in which the perturbations to the inclination, averaged over one orbit, are zero. Thus orbits with zero inclination relative to the Laplace plane remain nearly coplanar. Furthermore, those with nonzero inclinations precess about a vector normal to the Laplace plane under the influence of the combined force just as non-equatorial orbits precess about a planet's spin axis due to the oblateness force alone. The Laplace plane shares a line of nodes with both the equatorial and ecliptic planes and thus its location can be defined by a tilt—an inclination—relative to the equatorial plane. This inclination is, of course, i_{forced}, which depends only on the strength of radiation pressure and that of oblateness as it must. The parameter i_{free} is then the inclination of the orbit as measured from the Laplace plane. The correspondence between equatorial inclinations and nodes, and their Laplace equivalents, is demonstrated in Fig. 7.

A more mathematical, yet well-written and easy-to-follow, discussion of the conventional Laplace plane (that arising from the forces of planetary oblateness and solar gravity) is given by Dobrovolskis (1993). The Hamiltonian method that Dobrovolskis applies to the conventional problem can also be applied when radiation pressure is important since this force can also be derived from a potential (Hamilton and Burns 1992). The main difference between the two problems is that the acceleration induced by radiation pressure, unlike that from solar gravity, depends on particle size. Indeed, in the conventional case the Laplace plane for an orbit of given size is tilted by a constant amount while with radiation pressure the tilt is size-dependent. Thus grains of various sizes launched from Deimos oscillate about different Laplace planes.

3.2. Numerical Simulations

In quantitative tests, the solution given by Eqs. (20) and (21) fares very well. For 40 μm Deimos grains, we find $\alpha \approx 0.5392$, $\dot{\Omega}_{xy} \approx -0.1120$, $\dot{\tilde{\omega}}_{\text{T}} \approx -3.229$. The amplitude and period of the inclination predicted by these expressions are then 14° and 40 yr, respectively. These are in excellent agreement with the 13° and 39 yr seen in Fig. 7. Slight differences are due to the nonzero eccentricity in Eq. (14) and the neglected high-amplitude short-period terms. Considering the approximations made, however, the solution provides a very good guideline for the orbital evolution

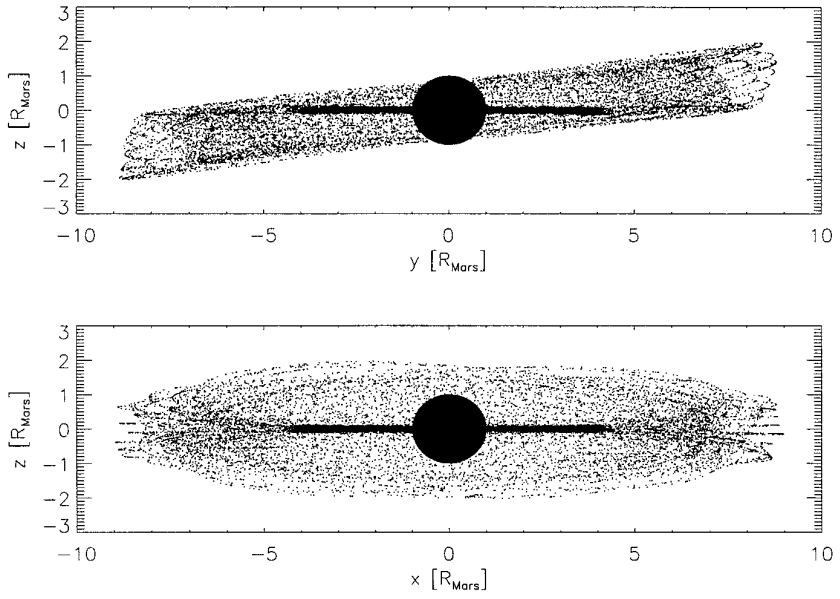

FIG. 8. Vertical structure of the 40 μm component of the martian rings. The coordinate system is centered on Mars and does not rotate; x is along the ascending node of the ecliptic on the equatorial plane (i.e., vernal equinox), y is also in the equatorial plane, and z is parallel to Mars' spin axis. The Phobos ring remains concentrated near the equatorial plane ($z = 0$) in both panels. When projected into the yz plane, the Deimos ring is tilted toward the ecliptic plane by $i_{\text{forced}} \approx 6.5°$. When projected into the xz plane, however, the ring is symmetric about the x-axis.

experienced by Deimos grains. But what is the vertical shape of the ring traced out by these particles?

The vertical distribution of 40 μm grains from both Phobos and Deimos is shown in the two panels of Fig. 8. As in Fig. 3, the orbits of two particles—one from Phobos and one from Deimos—have been followed for several tens of thousands of revolutions about Mars. Although this figure gives a rough approximation of what the 40 μm component of the martian rings looks like, it differs from a snapshot, as will be argued below. The Phobos contribution in both panels is confined to a thin band near the equatorial plane (in agreement with the low inclinations seen in Fig. 2), but the broader Deimos ring shows an interesting three-dimensional structure.

Using the intuition gained from the above discussion of the Laplace plane, we can understand the appearance of the ring created by 40 μm grains from Deimos. The Laplace plane intersects the ecliptic and equatorial planes at their common line of nodes and is tilted by i_{forced} from the equatorial plane. Particles oscillate about the Laplace plane with $i = i_{\text{free}}$ and precess at a uniform rate in this frame. As seen from along the common line of nodes, therefore, the ring should be tilted toward the ecliptic plane by an angle of i_{forced} (see first panel of Fig. 8). Moreover, it should appear roughly rectangular in cross section with a width of $\approx 2a(1 + e_{\max}) \sin i_{\text{free}} \approx 2R_{\text{mars}}$. Since $i_{\text{forced}} = i_{\text{free}}$ for our initial conditions, the inclination from the equatorial plane varies between 0° and $2i_{\text{forced}}$. Due to the ring's tilt, the nearly equatorial orbit of Deimos skirts the lower edge of the ring, rises through it, skims along the top edge, and finally descends through the ring. The second panel of Fig. 8 shows a view from the negative y-axis. The vertical asymmetry is not apparent from this angle, but the nonrectangular profile of the ring indicates dynamics more complicated than simple precession about the equatorial plane.

The simple analytic approximations given above qualitatively portray the type of orbital evolution displayed by small dust grains launched from Deimos. Numerical integrations, however, are needed for more quantitative studies and for Phobos grains which undergo more complicated oscillations. In particular, these simulations are required to assess the importance of effects not included in the analytic solution, namely launch at different seasons, the nonlinear e and i terms, and the 1° inclinations of Phobos and Deimos. The effects of the martian eccentricity will be discussed in Section 4.3. Figure 9 shows the results of nearly 500 numerical integrations; we plot both the maximum and minimum orbital inclinations attained by dust grains of different sizes launched from Phobos (panel 1) and Deimos (panel 2). As in Fig. 4, the solid lines pertain to particles launched in summer and winter while the dashed lines indicate grains started in spring and fall. Our analytic solution, shown as the dotted line for Deimos, gives slightly larger inclinations than our numerical simulations, but the curves are nevertheless in good agreement.

The discrepancies between particles launched at the equinoxes and those started at the solstices are clearly apparent, much more so than in Fig. 4. The largest differ-

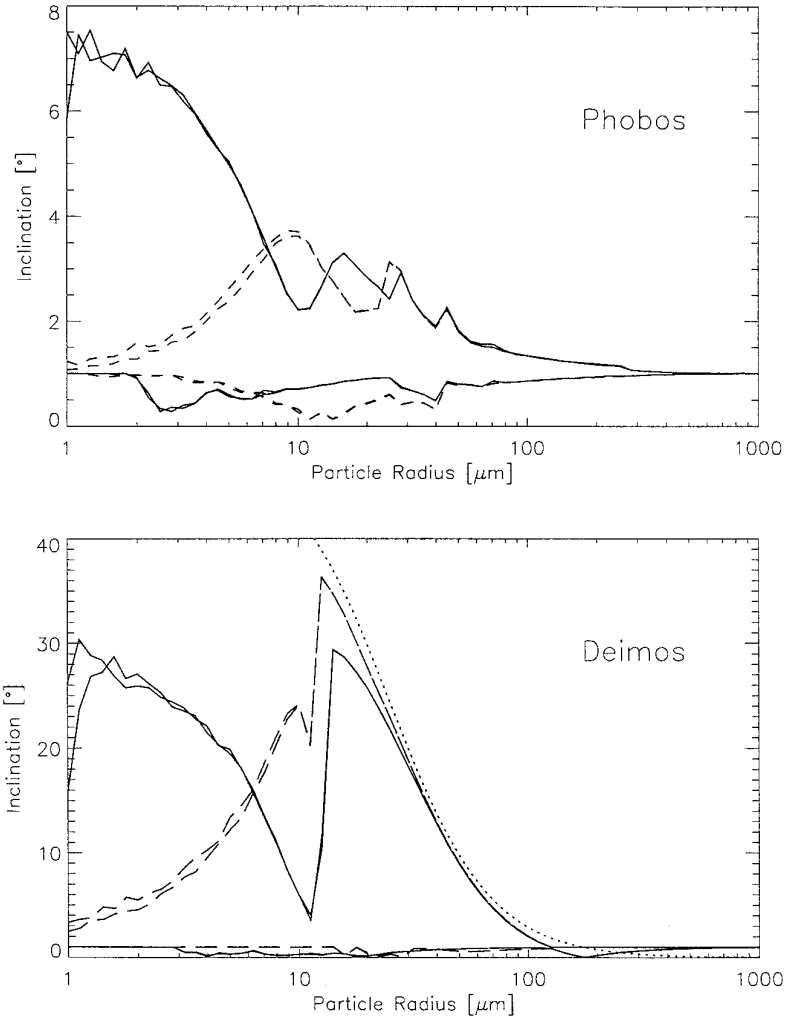

FIG. 9. Maximum and minimum inclinations of Phobos and Deimos ejecta as functions of particle size. As in Fig. 4, ejecta is launched in different seasons: summer and winter (solid curves) and spring and autumn (dashed curves). For Deimos, the analytic prediction of $2i_{\text{forced}}$ (Eq. 22) is indicated by the dotted curve. Strong seasonal differences occur for particles up to about 30 μm in radius. For particles above 300 μm, the 1° inclinations of the source satellites dominate over changes produced by radiation pressure. The sharp rises in the Deimos curves occur near $s_{\text{impact}} \approx 15$ μm when particles first avoid collision with Mars; such grains have much longer lifespans and achieve higher inclinations.

ences occur for particles with sizes less than s_{impact} (Table II), which strike Mars after a few years and hence do not contribute much to the ring's optical depth. For these short-lived particles, small differences between grains launched half a martian year apart are apparent, but for larger particles the two dashed curves in Fig. 9 merge, as do the two solid ones. The convergence of the similarly drawn curves indicates that the orientation of the moon's orbit, which changes due to nodal regression, is unimportant in determining the maximum inclinations attained by ejecta particles. Similarly, for grains larger than about 30 to 40 μm, the time of launch ceases to be important as indicated by the convergence of the solid and dashed lines. Finally, the vertical structure of the ring composed of particles greater than a few hundred micrometers in radius is dominated by the inclination of the source moonlet; radiation pressure can force only small fluctuations about this value.

4. SYNTHESIS: THE BIG PICTURE

4.1. Three-Dimensional Time-Variable Structure

In the previous sections, we have discussed the azimuthal and vertical structure of the Phobos and Deimos rings separately. Here we synthesize these results into a three-dimensional model of ring structure, first for a single particle size and then for multiple sizes. For Phobos, this synthesis is particularly simple since for particles large enough to avoid colliding with Mars ($s > s_{\text{impact}} \approx 26$ μm—see Table II), the ring's inclination is at most a few degrees. This corresponds to a thickness of only a few hundred

kilometers at Phobos's orbit, which is much smaller than the radial width arising from perturbations to the orbital eccentricity. Ignoring vertical variations at smaller length scales we find that, to a good approximation, the Phobos ring's three-dimensional shape is a very thin disk with a wedge-shaped cross section and the azimuthal structure discussed above.

The situation for Deimos, however, is more complicated. The Deimos ring, like the example for 40 μm grains shown in Figs. 3 and 8, can have both significant width and thickness. The full three-dimensional shape of the ring depends, therefore, on both the azimuthal and vertical perturbations. We can take advantage of the symmetries implicit in Figs. 3 and 8 to determine this shape. The azimuthal perturbation creates an asymmetric structure in a frame rotating with Mars' mean motion (Fig. 3); by contrast the vertical perturbation creates an asymmetric structure in the nonrotating frame (Fig. 8). Since the relation between these two frames varies periodically in time, the relation between the asymmetric features does too. In short, the ring's shape is a function of time, or more exactly, of the martian season. This time dependence is best illustrated by a few examples.

What would a spacecraft circling Mars on a distant equatorial orbit see just as it crossed over the dawn terminator? This corresponds to viewing the ring in Fig. 3 edge-on from the negative $y_{\rm rot}$-axis, so the spacecraft would certainly see a Deimos component extending further away from the Sun than toward the Sun. In addition, the vertical profile will vary with the season as the $y_{\rm rot}$-axis aligns with different nonrotating directions. In Fig. 10, we show the spacecraft's view of the ring in four different seasons. The first panel shows the ring at the spring equinox (in the northern hemisphere), which corresponds to rotating the Deimos ring in Fig. 3 through an angle $i_{\rm forced}$ around the positive $x_{\rm rot}$-axis. The part of the ring that appears to be above Mars in Fig. 10's first panel is further from the spacecraft than the planet, while the converse is true for material below Mars. For the summer solstice, autumn equinox, and winter solstice, the Deimos ring in Fig. 3 is rotated by $i_{\rm forced}$ around the negative $y_{\rm rot}$-axis, negative $x_{\rm rot}$-axis, and positive $y_{\rm rot}$-axis, respectively. Thus the elevated part of the ring varies with the season. As viewed from Mars' surface at the equator at local midnight, the ring would appear as a broadened great circle passing directly overhead in spring and autumn, but displaced to the south in summer and to the north in winter.

4.2. An Ensemble of Particle Sizes

In the previous sections, we have investigated the dynamics and structure of the Phobos and Deimos rings as if they were composed of only a single particle size. Here we discuss, in general terms, properties of superpositions of such rings formed by particles of different sizes launched from both moons.

We first focus on radial and azimuthal structure. Using the data from Fig. 4 with Fig. 3 as a guide, we can mentally build up a superposition of rings of different particles sizes: for each different particle size, we read off the maximum eccentricity and the orientation of the solar angle at maximum eccentricity. Figure 6 provides a guide for how ''nonlinear'' rings can look. Approaching Mars radially along the positive $x_{\rm rot}$-axis in Fig. 3, we encounter the orbit of Deimos and the full range of particle sizes all at once. Moving inward, the range of particle sizes narrows, as the larger grains are more closely bound to Deimos' orbit. At $4.5R_{\rm Mars}$, we reach the first Phobos grains, which have $s = s_{\rm impact} = 26$ μm; at this point, the largest Deimos grains are just under 40 μm in radius. Continuing inward, the Deimos grains become smaller and smaller, while the Phobos size distribution broadens rapidly. After crossing the Phobos orbit, this distribution narrows quickly until only the tiniest particles from both Phobos and Deimos are detectable.

Approaching along the negative $x_{\rm rot}$-axis of Fig. 3 is quite different. The tiniest Deimos particles are detected first, and the size distribution broadens until the largest particles are found at the orbit of Deimos itself. Crossing the orbit, particles larger than 20 μm or so disappear within a couple of tenths of a martian radius. Then comes a wide open space relatively void of sizable particles until Phobos grains larger than 270 μm appear at about $3.5R_{\rm Mars}$. Crossing Phobos' orbit, the big particles disappear and grains smaller than 270 μm show up. This distribution changes relatively slowly until the planet's surface is reached. Approaching from other directions compromises between the sunward and anti-sunward extremes. Small Deimos particles are encountered first, the distribution broadens until the Deimos orbit and then narrows back down to small particles. The same occurs as the Phobos ring is crossed.

The vertical structure is easier to understand. For the Phobos ring, all particles are encountered within a few hundred kilometers of the equatorial plane with larger particles slightly more concentrated toward that plane. For Deimos, Eq. (22) shows that particle sizes increase as the forced inclination decreases, and Eqs. (20) and (21) imply that all of the different Laplace planes and the equatorial plane intersect at the same line. Thus distributions equivalent to Figs. 8 and 10 for larger particles are simply thinner and less tilted. For Deimos, the season of observation also plays a role. Approaching the ring from above the negative $x_{\rm rot}$-axis (away from the Sun) in winter (bottom panel, Fig. 10), we would find a distribution composed of small particles first, gradually building up to all sizes, and then vanishing soon after crossing the equatorial plane. In summer, we would find the opposite—first the equatorial plane and a broad distribution, then smaller and smaller particles.

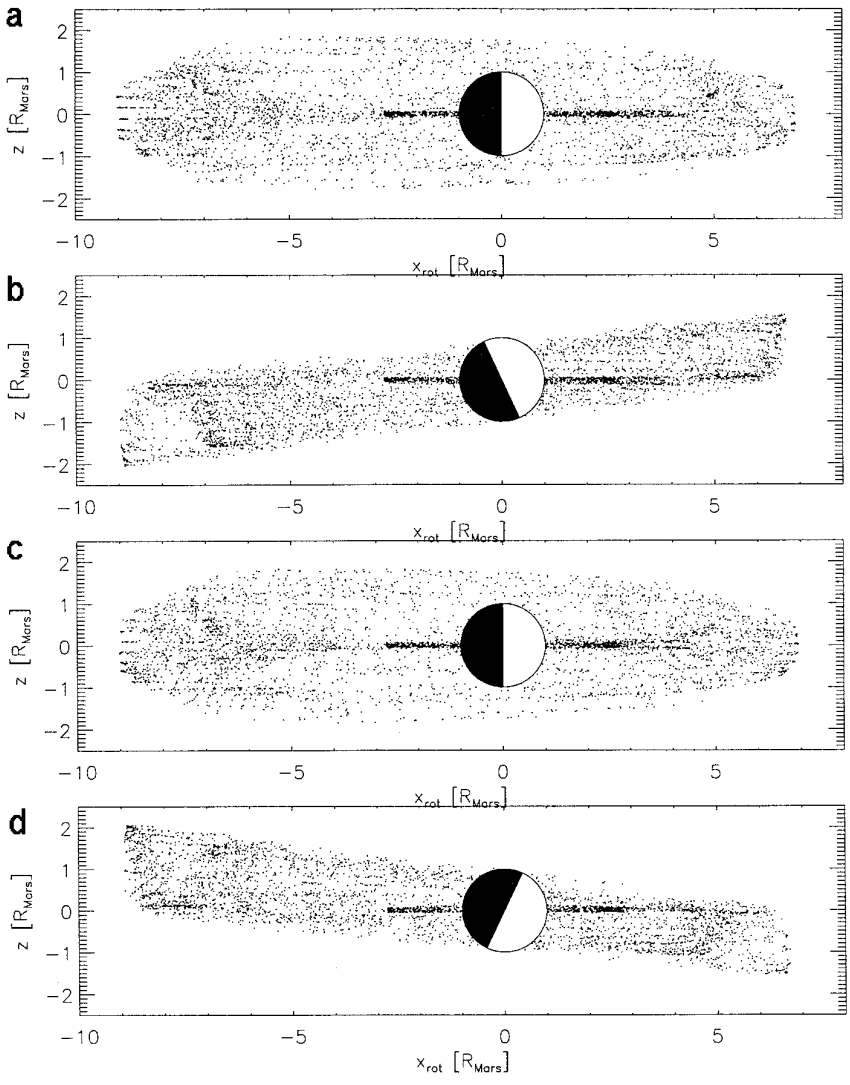

FIG. 10. Seasonal dependence of the 40 μm martian rings as seen from a point in the equatorial plane and above the dawn terminator. The four panels correspond to (a) the spring equinox, (b) the summer solstice, (c) the autumn equinox, and (d) the winter solstice in Mars' northern hemisphere. The position of the Sun, and hence the ecliptic, is indicated by the "lit" hemisphere of Mars. The Phobos ring remains concentrated to the equatorial plane in all seasons. The most distant Deimos particles are noticeably offset away from the Sun due to the azimuthal asymmetry (see Fig. 3). From this viewing angle, the ring formed by these particles appears to be symmetric about the equatorial plane during the equinoxes, but tilted out of this plane during the solstices.

During spring and autumn, larger particles are concentrated toward the equatorial plane and are surrounded by a halo of smaller grains.

4.3. Effects of the Martian Eccentricity

The preceding analytic and numerical results all apply to a circularly orbiting Mars, although we have stressed throughout that our results provide a reasonable guide for the general case. In this section, we discuss how our results are modified by the inclusion of the martian eccentricity.

In Section 2.1, we noted that the martian eccentricity causes periodic changes to α and $n_\odot$ which occur over a martian year. The changes in the eccentricities of grains from Deimos occur on a very similar timescale, so we might expect a long-period beat between the two periods. Our numerical investigations do indeed show beating in the eccentricity traces, typically with a small amplitude and a period of $\approx$100 years. This oscillation has several important effects. First, maximum eccentricities are increased slightly, which leads to a corresponding increase in $s_{\rm impact}$. In addition, the behavior of the oscillation in eccentricity is sensitive to the position of Mars in its orbit when the grains are launched which leads to a time-dependent $s_{\rm impact}$.

More seriously, since the dynamics are a function of the launch time, the structure of the Deimos ring for a given particle size should not be obtained by the orbit traced out by a single grain, but rather has to be built up from an ensemble of grains launched at different times. Furthermore, such orbits would need to be followed for centuries to include the effects of the beat period. Finally $e_{\text{free}} \neq e_{\text{forced}}$ which also changes the shape of the rings. The quantity e_{forced}, however, remains relatively constant and not very different from its value for $e_{\text{Mars}} = 0$ (Eq. 8). Thus the Deimos ring is not strongly affected and, in particular, will still be offset away from the Sun.

Juhasz and Horanyi (1995) have also studied the effects of the martian eccentricity on a small Deimos grain. They see a high-amplitude short-period beating in the orbital eccentricity (their Fig. 1) that is much larger than in our simulations, even after accounting for differences in the assumed mass density and Q_{pr}. Juhasz and Horanyi (1995) included the inverse-square dependence of radiation pressure on the Sun–Mars distance in their simulations, but assumed that Mars travels along its orbit at a constant angular rate rather than faster at pericenter and slower at apocenter (Juhasz, private communication, 1995). This approximation artificially enhances the effects of martian eccentricity.

Our numerical simulations also show only trivial changes in the vertical structure of the Deimos ring—at least on the short term. This can be understood analytically by considering the solution given by Eqs. (20) and (21). In the derivation of these equations we neglected short-period effects, and the changes introduced by the varying distance between Mars and the Sun is just another such term. Similarly, we see no significant effects in the eccentricity obtained by Phobos 250 μm grains since the long period of the eccentricity oscillation effectively averages over many circuits of Mars about the Sun.

For small Phobos grains, however, the ratio of the period of the eccentricity oscillation and Mars' orbital period can take on many values (Fig. 4). In addition, small changes in $n_{\odot}$ can drastically affect Eq. (9) due to the resonance condition, whereas the changes to Eq. (10) are slight. We thus expect to see all of the effects discussed for Deimos occurring more rapidly and on a larger scale at Phobos. Indeed, in our simulation of Phobos 40 μm grains (Fig. 11), we see double-lobed eccentricity peaks which are the result of the similarity between the eccentricity oscillation and the martian year. Our 40 μm example crashed into Mars after about 20 years, which indicates that the time-dependent s_{impact} for Phobos can differ significantly from its value for $e_{\text{Mars}} = 0$. This behavior also implies that an ensemble of particles launched at different times is necessary to accurately characterize the structure of the Phobos ring.

Although the details of individual orbits differ and the value of s_{impact} is raised (perhaps significantly for Phobos), most features of the $e_{\text{Mars}} = 0$ solution are retained. In particular, Deimos rings will still be offset away from the Sun and tilted at a compromise angle between the equatorial and ecliptic planes. Since the quantities determining these offsets, e_{forced} and i_{forced}, are not significantly influenced by the addition of the martian eccentricity, even the magnitudes of the asymmetries will be relatively unchanged. The Deimos ring still exhibits seasonal changes when $e_{\text{Mars}} \neq 0$. For Phobos, e_{forced} will be affected more strongly, resulting in greater differences. Nevertheless, the Phobos ring will still be offset away from the Sun for grains smaller than $\approx$270 μm. In short, the gross features of the ring are relatively unaltered by the martian eccentricity and the model presented above gives a good first-order solution for its three-dimensional structure.

4.4. Collisional Processes; Optical Depth

The dynamics of dust in orbit around Mars is complicated, yet relatively straightforward to determine with the numerical and analytic methods that we have discussed above. But dynamics determines only the three-dimensional structure of the rings; the steady-state size distribution of particles present in the ring also depends strongly on the details of the sources and sinks for dust around Mars.

The main sinks for Martian dust are simple to understand and model since they depend only on the dynamics. They are (1) collisions with Mars, (2) collisions with the moons, (3) mutual collisions, and (4) escape. Particles smaller than a micrometer are rapidly blown away from Mars by the solar wind, grains smaller than s_{impact} crash into Mars within a few years, and all remaining Phobos grains are reabsorbed by that moon in 30 to 70 yr (Table I). Deimos grains larger than s_{impact}, by contrast, can live for 2000 to $\approx$25,000 years. Recollision with the source satellite is roughly independent of the orbital eccentricity and increases nearly linearly with inclination for moderate inclinations (Hamilton and Burns 1994). Deimos grains in the size range between s_{impact} and s_{cross} (Table II) are reabsorbed by both Phobos and Deimos. Clearly if all sizes were produced in equal numbers, Deimos grains in the s_{cross} size range would dominate martian cicumplanetary space.

The sources, however, greatly complicate the problem of predicting the size distribution in the rings. They are, however, easy to enumerate: (1) Collisional ejecta from the impact of interplanetary particles onto Phobos and Deimos and (2) Collisional ejecta from reimpacting ring particles. The first of these sources has been treated in detail by Juhasz *et al.* (1993), Juhasz and Horanyi (1995), Ishimoto and Mukai (1994), and Krivov (1994). Uncertainties arise in the size distribution of incoming particles (see Grün *et al.* 1985) and especially in accurately determining the amount and size distribution of the escaping ejecta for

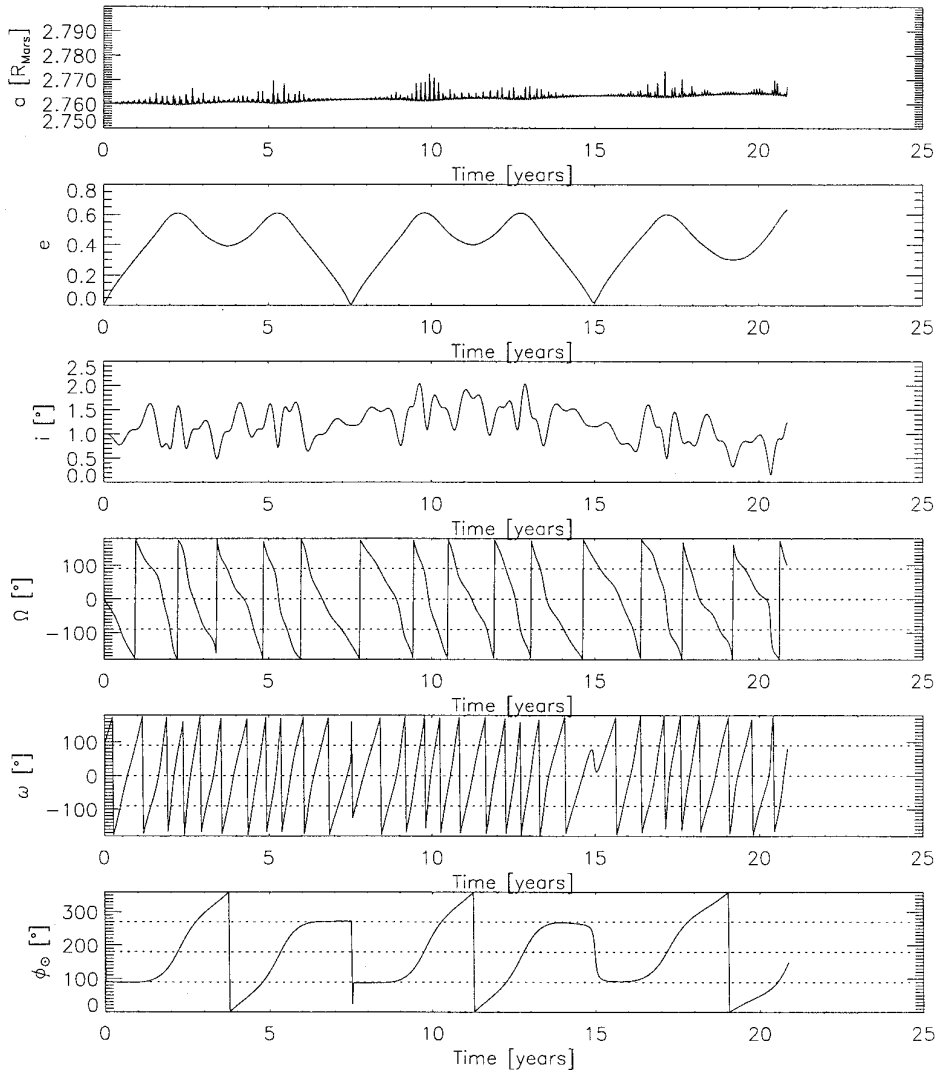

FIG. 11. The orbital history of a 40 μm grain launched from Phobos. All start parameters are identical to those in Fig. 2, except here we include the martian eccentricity and start Mars at its pericenter. Compare the eccentricity and solar angle profiles with those of Fig. 2.

a given impact. Both quantities depend strongly on details of the satellite's surface composition and regolith which are poorly known. For example, using different assumptions for these properties, Juhasz *et al.* (1993) and Ishimoto and Mukai (1994) find source rates from Phobos that differ by up to two orders of magnitude. Nevertheless, both groups proceeded to derive rough size distributions expected in the martian rings. These distributions should be used with caution since (1) there are large uncertainties in the source strength, (2) the dynamics used neglect the important perturbations of the martian oblateness and eccentricity, and (3) incorrect recollision timescales were used. Juhasz and Horanyi (1995) correct the second and third points in their study of small Deimos dust grains.

Instead of interplanetary particles, we focus on the second possibility: reimpacting ring particles. Sasaki (1992) first suggested that these impacts might enhance the population of the martian dust rings. If the impact of a ring particle with a moon is energetic enough, then ejecta in the size-range of the impacter might be liberated from the moon's surface. With enough of this ejecta, the ring enjoys a net gain of material. Such a ring would increase in optical depth until mutual collisions began to destroy significant numbers of dust grains before they recollided with the moon (Hamilton and Burns 1994). A steady-state self-sustaining ring is the endpoint of this evolution and is typically reached in several tens of collisional timescales (Table I). Hamilton and Burns (1994) argue that this process dominates in Saturn's E ring.

Deciding whether or not this process occurs at Mars is complicated by our lack of knowledge of the amount and size distribution of escaping ejecta from a given impact. It

is insufficient to simply compare the typical impact velocities, as Juhasz and Horanyi (1995) do, since this neglects impact rates which heavily favor martian debris. We can only make general arguments and discuss the possible consequences. The large eccentricity component of the martian rings is most likely to be self-sustaining since collision velocities are approximately $ev_{\rm circ}$ (Hamilton and Burns 1994). Thus it is most probable for Deimos grains larger than $s_{\rm impact}$ which reimpact Deimos at speeds of up to 1 km/s, and for Phobos grains between $s_{\rm impact} \approx 26\ \mu$m and $s_{\rm crit} \approx 270\ \mu$m which reimpact at up to 1.4 km/s. These speeds are about two orders of magnitude higher than the satellite escape velocities (Table I), a ratio similar to that in Saturn's E ring (Hamilton and Burns 1994). Thus only a few tenths of a percent of the impact's kinetic energy needs to be channeled into the kinetic energy of similar-sized fragments. On the negative side, collisions at sub-km/sec speeds are not especially efficient at fracturing rocky targets. We cannot, therefore, be certain that the rings are self-sustaining. Nevertheless, we forge ahead and investigate the consequences that arise if this is indeed the case.

In the self-sustaining scenario, like any other collision process, the smallest ejecta fragments are favored since they are far more numerous. Thus particles slightly larger than $s_{\rm impact}$ dominate the Phobos and Deimos rings in both the self-sustaining and interplanetary-collision models. What differs are the predicted optical depths. The optical depth of a self-sustaining ring can be roughly estimated. If one impact creates N similar-sized ejecta particles then, in steady state, $N - 1$ of these are lost to mutual collisions and one makes it back to the moon to repeat the process. Thus the ratio of the total cross-sectional area of all the ring particles to the source satellite is $(N - 1)/2$, where the 2 comes from the fact that two ring particles are destroyed in each mutual collision. This leads to an approximate expression for the self-sustained optical depth

$$\tau_{\rm ss} = (N-1)\,\frac{R_{\rm moon}^2}{4a^2 e_{\rm max}} \qquad (23)$$

with $N > 1$. Note that the expression is independent of the size of the ring particles. We now assume, based on the above discussion, that the ring just barely self-sustains and take $N = 2$ (i.e., one impacter produces two ejecta particles of a similar size). With these assumptions, we find $\tau_{\rm ss} \approx 8 \times 10^{-7}$ for the Phobos ring and $\tau_{\rm ss} \approx 5 \times 10^{-8}$ for the Deimos ring. Sasaki (1994) has obtained similar results for Phobos. These values are 100–1000 times smaller than the upper limit established by Viking (Duxbury and Ocampo 1988) but far larger than those expected for production dominated by interplanetary particles.

4.5. Possibilities for Observation

The hypothetical martian dust halo bears the dubious distinction of being the longest-studied ring whose existence has yet to be verified; here we briefly consider the possibilities for successful observations in the near future. Spacecraft missions to Mars provide the best opportunity for detecting the rings either photographically or by particle impacts. The Japanese Planet B mission, for example, will carry a dust detector to Mars in 1999 (Ishimoto and Mukai 1994, Ishimoto *et al.* 1994). Since numbers rather than cross-sectional areas are important for impacts, the instrument will predominantly see small particles. The flux of these grains will vary azimuthally, vertically, and temporally. In addition, if the martian rings are self-sustaining, the spacecraft will occasionally meet a large dust grain. The number density of $\approx$50 μm particles near Phobos is perhaps as high as 10^{-3} m^{-3}. These grains offer the best chance for the first measurement of the electrical charge on a cosmic body since the charge on a grain should increase roughly linearly with its radius. In addition, charging currents near Mars are interesting: Juhasz and Horanyi (1995) argue that the charge on a particle varies immensely as it moves in and out of the martian bow shock. Spacecraft could provide *in situ* measurements capable of elucidating this phenomenon. We note that 50 μm particles should not prove a significant threat to an orbiting spacecraft since impact velocities are relatively low.

Finally, we comment on the possibility of detecting the rings from the Earth. Several groups have attempted to detect faint martian rings from the ground without success, but the apparent brightness of these faint rings varies strongly with the viewing geometry. The best time to look for faint rings are (1) when Mars is near opposition, (2) when Mars is near its orbital pericenter, and (3) when the rings appear almost edge-on as seen from Earth (as do the rings of Saturn in 1995). For the Phobos ring, the best combination of these parameters in the next 35 yr occurs in early June 2001, when the ring opening angle will less than a degree and Mars will be about 0.47 AU from Earth. At this time, the putative ring should be at least a magnitude brighter than at any time in the 1990s. If we assume the value of $\tau_{\rm ss} = 8 \times 10^{-7}$ for the Phobos ring and take nominal parameters for 50–200 μm grains, we estimate that a one square arcsecond patch of sky near Phobos' orbit should appear approximately five magnitudes fainter than Phobos at that time. If the ring is not self-sustaining, however, its apparent brightness will be substantially lower.

5. CONCLUSION

In this paper, we have presented a detailed investigation of the dynamics of martian dust grains between 1 μm and 1000 μm in radius. We have modeled the complicated interplay between solar radiation pressure and the martian oblateness force using both analytic and numerical techniques. Our analyses show that the eccentricity and obliquity of Mars significantly influence the structure of the

martian rings. Shadowing by the planet and the initial inclinations for Phobos and Deimos are less important. Many of the usual symmetries displayed by planetary rings are invalid for dust around Mars. The martian rings are azimuthally asymmetric: Deimos dust is offset away from the Sun while Phobos dust is found primarily in the solar direction. Dust grains from Deimos oscillate about size-dependent Laplace planes, which creates a vertically asymmetric ring. For the Deimos ring, the interaction between the two asymmetries gives rise to a time-dependent structure that varies with the martian season.

Despite the complications that arise when two perturbations are nearly equal in strength, we find that a simple analytic model based on forced eccentricities (Eqs. (6) and (7)) and inclinations (Eqs. (20) and (21)) well approximates the dynamics of martian ring particles. For a circularly orbiting Mars, the model can be extended to large eccentricities and inclinations by using the numerically determined parameters displayed in Figs. 4 and 9. The rings created by individual particles of different sizes may then be superposed to approximate the time-variable structure of the martian rings. Because Mars has a reasonably elliptic orbit, however, a beat between two frequencies arises which subtly alters the dynamics. Even in this case, however, our model still serves as a reasonable approximation.

The martian rings may be self-sustaining. If they are, rings composed of large particles (20–300 μm) could be detected *in situ* and possibly even from ground-based telescopes. If the rings do not sustain themselves, the dominant population of particles will probably be small (<30 μm) temporary residents of the martian system, destined either to stream away from Mars or to strike the planet at the whim of solar radiation and electromagnetic forces.

ACKNOWLEDGMENTS

I thank Klaus Richter and an anonymous reviewer for their detailed comments. This work was supported by an NSF/NATO postdoctoral fellowship and by a Max Planck visitor's grant.

REFERENCES

Adolfsson, L. G., B. A. S. Gustafson, and C. D. Murray 1996. The martian atmosphere as a meteoroid detector. *Icarus,* **119,** 144–152.

Allan, R. R., and G. E. Cook 1967. Discussion of paper by S. J. Peale, "Dust belt of the Earth." *J. Geophys. Res.* **72,** 1124–1127.

Banaszkiewicz, M., and W.-H. Ip 1991. A statistical study of impact ejecta distribution around Phobos and Deimos. *Icarus* **90,** 237–253.

Burns, J. A., L. E. Schaffer, R. J. Greenberg, and M. R. Showalter 1985. Lorentz resonances and the structure of the jovian ring. *Nature* **316,** 115–119.

Danby, J. M. A. 1988. *Fundamentals of Celestial Mechanics* (2nd ed.). Willmann–Bell, Richmond, VA.

Davis, D. R., K. R. Housen, and R. Greenberg 1981. The unusual dynamic environment of Phobos and Deimos. *Icarus* **47,** 220–233.

Dobrovolskis, A. R. 1993. The Laplace planes of Uranus and Pluto. *Icarus* **105,** 400–407.

Dobrovolskis, A. R., and J. A. Burns 1980. Life near the Roche limit: Behavior of ejecta from satellites close to planets. *Icarus* **42,** 422–441.

Dubinin, E. M., R. Lundin, N. F. Pissarenko, S. V. Barabash, A. V. Zakharov, H. Koshinen, K. Schwingenshuh, and Ye. G. Yeroshenko 1990. Indirect evidence for a gas/dust torus along the Phobos orbit. *Geophys. Res. Lett.* **17**(6), 861–864.

Duxbury, J. C., and A. C. Ocampo 1988. Mars: Satellite and ring search from Viking. *Icarus* **76,** 160–162.

Grün, E., H. A. Zook, H. Fechtig, and R. H. Giese 1985. Collisional balance of the meteoritic complex. *Icarus* **62,** 244–272.

Hamilton, D. P. 1993. Motion of dust in a planetary magnetosphere: Orbit-averaged equations for oblateness, electromagnetic, and radiation forces with application to Saturn's E ring. *Icarus* **101,** 244–264. Erratum: *Icarus* **103,** 161.

Hamilton, D. P., and J. A. Burns 1992. Orbital stability zones about asteroids. II. The destabilizing effects of eccentric orbits and of solar radiation. *Icarus* **96,** 43–64.

Hamilton, D. P., and J. A. Burns 1994. Origin of Saturn's E ring: Self-sustained, naturally. *Science* **264,** 550–553.

Horanyi, M., and J. A. Burns 1991. Charged dust dynamics: Orbital resonance due to planetary shadows. *J. Geophys. Res.* **96,** 19,283–19,289.

Horanyi, M., J. A. Burns, M. Tatrallyay, and J. G. Luhmann 1990. Toward understanding the fate of dust lost from the martian satellites. *Geophys. Res. Lett.* **17,** 6, 853–856.

Horanyi, M., M. Tatrallyay, A. Juhasz, and J. G. Luhmann 1991. The dynamics of submicron-sized dust particles lost from Phobos. *J. Geophys. Res.* **96,** 11,283–11,290.

Horanyi, M., J. A. Burns, and D. P. Hamilton 1992. The dynamics of Saturn's E ring particles. *Icarus* **97,** 248–259.

Ishimoto, H. 1995. Formation of Phobos/Deimos dust rings. *Icarus,* in press.

Ishimoto, H., and T. Mukai 1994. Phobos dust rings. *Planet. Space Sci.* **42,** 691–697.

Ishimoto, H., H. Kimura, N. Nakagawa, and T. Mukai 1994. Planned observation of Phobos/Deimos dust rings by Planet-B. *Adv. Space Res.,* submitted.

Juhasz, A., and M. Horanyi 1995. Dust torus around Mars. *J. Geophys. Res.* **100,** 3277–3284.

Juhasz, A., M. Tatrallyay, G. Gevai, and M. Horanyi 1993. On the density of the dust halo around Mars. *J. Geophys. Res.* **98,** 1205–1211.

Kholshevnikov, K. V., A. V. Krivov, L. L. Sokolov, and V. B. Titov 1993. The dust torus around Phobos orbit. *Icarus* **105,** 351–362.

Krivov, A. V. 1994. On the dust belts of Mars. *Astron. Astrophys.* **291,** 657–663.

Krivov, A. V., L. L. Sokolov, and V. V. Dikarev 1995. Dynamics of Mars-orbiting dust: Effects of light pressure and planetary oblateness. *Celest. Mech. Dynam. Astron.,* submitted.

Mignard, F. 1984. Effects of radiation forces on dust particles in planetary rings. In *Planetary Rings* (R. Greenberg and A. Brahic, Eds.), Univ. of Arizona Press, Tucson, pp. 333–366.

Sasaki, S. 1992. Formation and development of martian dust rings. *Bull. Am. Astron. Soc.* **25,** 1107–1108.

Sasaki, S. 1994. Martian dust tori formation: Ejecta at collision of torus particles with the satellite can sustain dust abundance. In *Proceedings of 27th ISAS Lunar and Planetary Symposium* (M. Shimizu and H. Mizutani, Eds.).

Soter, S. L. 1971. *The Dust Belts of Mars.* Cornell Center for Radiophysics and Space Research Report 462.